RESEARCH ARTICLE | MARCH 05 2025

Time-frequency vortex characterization in large-scale experimental downbursts

Special Collection: Recent Fluid Mechanics: Celebrating the 100th Anniversary of the ICTAM (International Congress of Theoretical and Applied Mechanics)

Federico Canepa ; Hao-Yu Bin ; Stefano Brusco

Physics of Fluids 37, 036610 (2025)
https://doi.org/10.1063/5.0255845

Physics of Fluids ARTICLE pubs.aip.org/aip/pof

Time-frequency vortex characterization in large-scale experimental downbursts

Cite as: Phys. Fluids **37**, 036610 (2025); doi: 10.1063/5.0255845
Submitted: 31 December 2024 · Accepted: 12 February 2025 ·
Published Online: 5 March 2025

View Online Export Citation CrossMark

Federico Canepa,[1,a)] Hao-Yu Bin,[1] and Stefano Brusco[2]

AFFILIATIONS

[1]Department of Civil, Chemical and Environmental Engineering (DICCA), Polytechnic School, University of Genoa, Via Montallegro 1, 16145 Genoa, Italy
[2]Boundary Layer Wind Tunnel Laboratory, Faculty of Engineering, Western University, London, Ontario N6A 5B9, Canada

Note: This paper is part of the Special Topic, Recent Fluid Mechanics: Celebrating the 100th Anniversary of the ICTAM (International Congress of Theoretical and Applied Mechanics).
[a)]**Author to whom correspondence should be addressed:** federico.canepa@unige.it

ABSTRACT

Thunderstorms are severe atmospheric events with dramatic impacts on the Earth's surface. Among their various effects, downburst winds are especially significant, comprising a descending cold downdraft from the thunderstorm cloud and a horizontal outflow upon ground impact. The primary vortex dominates this flow in both stages, producing the highest near-ground velocities and forces. Due to the spatial and temporal transience of downbursts, experimental replication in specialized laboratories is essential for accurately investigating their dynamics. While traditional velocity measurements with Cobra probes offer high temporal resolution and a good spatial depiction of storm evolution through strategic instrument positioning and experimental repetitions, they often lack insights into the geometric and energetic characteristics of vortex structures and their correlation with recorded velocity signals. This paper addresses this gap through a time-frequency analysis of an extensive dataset of experimental downburst signals obtained at the WindEEE Dome simulator, Western University, Canada. The experimental configurations include isolated stationary downbursts, interactions with horizontal background wind within the atmospheric boundary layer, and effects of cloud motion on outflow patterns. The resulting asymmetry in horizontal outflow near the ground is captured through multiple Cobra probes positioned radially and azimuthally in the testing chamber. The continuous wavelet transform technique is applied to track the temporal evolution of energy content in downburst winds across the different simulated scenarios.

I. INTRODUCTION

Future climate projections indicate a marked increase in the frequency of thunderstorm events, particularly in regions considered "hot spots" for their genesis and development (Allen, 2018; Rädler *et al.*, 2019). These areas are often characterized by the presence of large water bodies, which supply the warm, moist air necessary to fuel storm systems. When this air interacts with colder inland currents, it generates energy that drives storm intensification. Among the phenomena arising from thunderstorms are downbursts, intense convective wind systems formed by buoyantly descending cold air (the downdraft) from cumulonimbus clouds that vertically pierce the lower levels of the atmospheric boundary layer (ABL), disrupting its stability. The instability at the radial interface between the downdraft and the surrounding environment produces vortical structures. The largest and most intense of these is named the primary vortex (PV), which leads the downdraft to the ground. Upon impingement, the PV propagation pulls the downburst flow radially outward at the near-ground level and causes the maximum wind speed between the vortex lower end and the ground (Lombardo *et al.*, 2014; Canepa *et al.*, 2022b). Smaller and weaker trailing vortices (TVs) follow the PV in space and time as long as the downdraft persists. The downdraft's strength and duration are indirectly influenced by the updraft intensity of warm, moist air feeding the cumulonimbus cloud, which can extend vertically from 1 to 2 km above ground to the tropopause (11–13 km). Additionally, the size and weight of hydrometeors (rain or hail) released from the cloud significantly affect the downdraft's momentum. The transiency of the phenomenon gives rise to highly non-stationary and non-Gaussian wind speed records, whose characteristics are strictly dependent on the event under consideration (Burlando *et al.*, 2018; Lombardo and Zickar, 2019; and Canepa *et al.*, 2020). The very limited space and time extension of the phenomenon—developing over a few

kilometers on the horizontal and spanning a duration from minutes to tens of minutes—makes the available records in nature still very limited compared to other types of stationary and large-scale windstorms, such as extra-tropical cyclones. It follows that the characterization and modeling of this type of phenomenon are still very limited to be properly represented in design codes. However, the recent emergence of advanced large-scale wind simulators capable of reproducing such kinds of extreme events has enabled groundbreaking experimental studies of downburst dynamics. In this context, the WindEEE Dome at Western University in Canada represents a one-of-a-kind laboratory (Hangan *et al.*, 2017). Here, an extensive experimental campaign at large geometric scales was conducted in 2019 and focused on characterizing downburst winds and the complex interactions that drive the phenomenon in nature. Particularly, these involve the coupling with the background horizontal wind in the ABL and the tilting of the downdraft axis due to cloud motion. These effects disrupt the radial symmetry of downburst outflows, as described by Fujita (1985), and produce intricate fluid dynamics, recently detailed in a series of studies by Canepa *et al.* (Canepa *et al.*, 2022a, 2022b, 2023) along with a database of measurements (Canepa *et al.*, 2022c). The experimental campaign also addressed the susceptivity of transient downburst flows and vortex structures to ground roughness (Canepa *et al.*, 2024a), a key parameter in the governing equations of stationary extra-tropical cyclones' winds. These interplays shape the near-ground dynamics, including the detachment–reattachment of the boundary layer at the surface, which forms a secondary counter-rotating vortex (SV) preceding the PV at further radial locations from the downdraft touchdown (Canepa *et al.*, 2022b).

Traditional wind speed analyses, typically performed in the time or frequency domain, have shed light on mean and turbulent flow components (Solari *et al.*, 2015; Zhang *et al.*, 2018) and their evolution with respect to the physical interpretation of the phenomenon (Canepa *et al.*, 2020, 2022b). Such an approach has allowed to relate the sudden ramp-up and peak of the velocity signal to the passage of the PV over the measuring instrument. The PV recording by the instrument represents a deterministic treat of the velocity signal and is characterized by quite limited turbulent fluctuations. The following TVs generate a sort of plateau of velocity with larger symmetric fluctuations around its mean value. When the downburst dissipates its energy, or moves away from the recording instrument, the wind speed gains turbulence but gradually ramps down to magnitudes preceding the onset of the PV, characterizing the background ABL horizontal flow. However, the time-domain analysis alone cannot fully capture the transient and complex nature of non-stationary events like downbursts. The use of power spectra provides frequency-specific insights of the velocity turbulent component but lacks temporal resolution, making it challenging to link energy content to specific flow structures. On the contrary, the use of time-frequency analyses permits to pursue this scope. In particular, the continuous wavelet transform (CWT) appears to be a suitable tool, as shown by Brusco *et al.* (2022a) by analyzing anemometric measurements associated with downburst wind speed signals acquired on the Italian north-west coast.

In this study, we adopt the continuous wavelet transform to analyze a large database of downburst wind speed signals from the WindEEE Dome. This approach allows for simultaneous time-frequency analysis, enabling a detailed examination of the evolving energy contributions from vortical structures and turbulent components. The CWT can also identify high-energy time intervals unrelated to vortical structures, providing new insights into transient flow dynamics beyond conventional metrics like turbulence intensity, even when defined as a time-varying quantity. This study presents a novel contribution by analyzing the time-evolving harmonic content associated with large-scale controlled downburst simulations. This approach enhances the assessment of atmospheric conditions and interactions that contribute to the development of high-energy, high-intensity extreme wind events, which, in turn, pose significant environmental hazards. Furthermore, it provides valuable insights into the geometry and dimensions of the leading downburst vortices, which would otherwise be overlooked by conventional pressure probe analysis. The findings have important implications for both structural engineering and atmospheric dynamics. From an engineering perspective, they help identify geometric and dynamic parameters that cannot be captured through conventional time-domain analysis. From an atmospheric dynamics standpoint, they provide insights into flow interactions that may lead to potentially hazardous conditions.

The remainder of this paper is organized as follows: Sec. II details the experimental setup and downburst configurations at the WindEEE Dome, as well as the wavelet analysis methodology. Section III presents the results, focusing on the energy evolution associated with PV propagation and turbulence. Finally, Sec. IV summarizes the findings and discusses prospects for future research.

II. EXPERIMENTAL SETUP AND METHODOLOGY

A. The WindEEE Dome and downburst generation

The WindEEE Dome is a large-scale, three-dimensional wind simulator designed to replicate various non-stationary wind systems, including downbursts, tornadoes, gusts, sheared and veered flows, and atmospheric boundary layers (Hangan *et al.*, 2017). The facility features a hexagonal testing chamber measuring 25 m in diameter and 3.8 m in height, surrounded by an outer return circuit with a 40 m diameter. Within the chamber, 100 fans are installed along the six peripheral walls. Among these, the 60-fan wall consists of a 4-by-15 matrix of 0.8 m diameter fans [Fig. 1(a)], enabling the generation of ABL-like flows. Downburst-like impinging jets are created using an upper chamber [Fig. 1(b)] housing six larger fans, each with a diameter 2.5 times that of the 60-fan wall fans (2.0 m). This upper chamber is connected to the testing area through a bell mouth. To generate the dynamic impinging jet (IJ), the six upper fans pressurize the chamber to a level approximately 3.4 hPa higher than the pressure in the testing chamber while the bell mouth louvers remain closed. When the desired pressure is reached, the louvers are suddenly opened, releasing the pressurized air downward into the testing chamber [Fig. 1(d)]. The bell mouth diameter (D) can be adjusted between 4.5 and 1.2 m by attaching different-sized rings. This flexibility allows the WindEEE Dome to simulate downburst-like outflows at various geometric scales, ranging from approximately 1:100 to over 1:1000 (Junayed *et al.*, 2019; Romanic *et al.*, 2020), and consequent large Reynolds numbers Re in the order of 10^6, with adjustable height-to-diameter (H/D) ratios.

B. Experimental setup

The experimental campaign at the WindEEE Dome investigated four experimental cases to examine various downburst scenarios: (i)

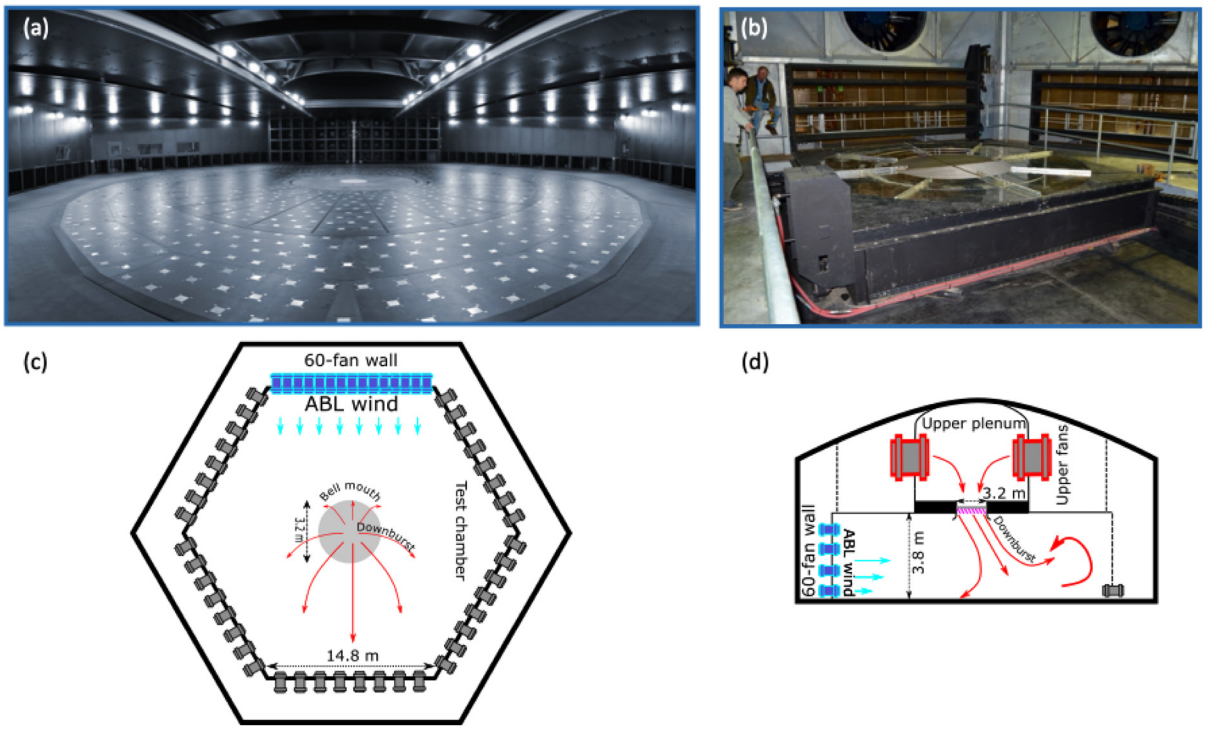

FIG. 1. Photograph of testing chamber (a) and upper plenum (b). Schematics of downburst generation with inclined jet axis from horizontal (c) and vertical (d) view.

vertical downburst (DB), hereafter named vertDB (Canepa *et al.*, 2022c, 2022b; 2024a); (ii) vertical downburst embedded in ABL flow (vertDBABL) (Canepa *et al.*, 2022a); (iii) inclined downburst (inclDB) (Canepa *et al.*, 2023); and (iv) inclined downburst embedded in ABL flow (inclDBABL) (Canepa *et al.*, 2023). Figures 1(c) and 1(d) schematically depicts the case inclDBABL.

In all configurations, the bell mouth diameter was $D = 3.2$ m, ensuring a height-to-diameter ratio $H/D > 1$ that allows to neglect confinement effects on the wall-jet outflow and particularly on the PV expansion (Junayed *et al.*, 2019). Based on D, the resulting length scale λ_L ranges from 1:200 to 1:300, corresponding to a microburst event (Fujita, 1985; Hjelmfelt, 1988). For generating the IJ and ABL flows, the upper plenum and the 60-fan wall fans were operated at 30% of their nominal power. This setup produced an IJ speed of $w_{IJ} = 12.4$ m s^{-1} at the bell mouth outlet and a horizontal flow speed of $u_{ABL} = 3.9$ m s^{-1} measured at a height $z = 0.25$, 3 m downstream of the 60-fan wall, for cases involving the ABL flow (Romanic *et al.*, 2019). Unlike classic boundary layer wind tunnels, where ABL profiles naturally develop along the tunnel fetch by means of active and passive control devices, the WindEEE Dome mechanically generates ABL-like flows by modulating the fan RPMs of the 60-fan wall. While the resulting turbulent profile differs from ESDU standards (i.e., ESDU, 2002), Romanic and Hangan (2020) argued that it closely resembles unstable atmospheric conditions typically observed prior to downburst events in nature. Additional velocity scales were also tested: $w_{IJ} = 8.9$ m s^{-1} for vertDB and $u_{ABL} = 2.5$ m s^{-1} for vertDBABL. Due to the closed-loop nature of the WindEEE Dome, including background horizontal velocities led to a reduction in the centroid jet velocity to $w_{IJ} = 11.8$ m s^{-1} for higher ABL speeds (Romanic *et al.*, 2019). However, corresponding data for lower ABL fan speeds is unavailable. For the cases inclDB and inclDBABL, the jet axis was inclined to $\theta = 30°$ from the vertical direction (toward the same direction of ABL blowing), consistent with the range of tilting angles at the ground observed in full-scale downburst outflows, for instance by Fujita (1985). Through simple trigonometry, this inclination introduced an additional horizontal velocity component of $V_S = 6.2$ and 5.9 m s^{-1} for inclDB and inclDBABL, respectively. These values represent the storm or cloud translation velocity in natural settings considering a velocity scale $\lambda_V = 1{:}1$–$1{:}1.5$, aligning well with radar observations of downburst cloud motion (Fujita, 1985). Combining geometric and velocity scales yielded a time scale λ_T approximately between 1:100 and 1:200.

For vertDB, tests were performed over three rough surfaces: (i) WindEEE Dome bare floor; (ii) carpet; and (iii) artificial grass. An equivalent roughness length $z_{0,eq}$ was determined for each surface, including the bare floor, which features irregularities across the surface. These values were derived from ABL-only simulations as described in detail in Canepa *et al.* (2024a). Using a length scale $\lambda_L = 1{:}200$, which proves to be adequate for both downburst and ABL reproductions at the WindEEE Dome, the resulting $z_{0,eq}$ values were 0.007 m (short vegetation), 0.02 m (cultivated areas with scattered obstacles or medium crops), and 0.32 m (rough surfaces like forests or suburban areas), corresponding to ESDU classifications (ESDU, 2002). These sub-cases are hereafter denoted as (i) vertDB007; (ii) vertDB020; and (iii) vertDB320, respectively.

Velocity records were acquired by means of Cobra probes (Turbulent Flow Instrumentation Pty Ltd), which are multi-hole

pressure sensors capable of measuring the three velocity components (u, v, and w) and static pressure in real-time. The output raw voltage is proportional to the pressure at the probe's head and is converted into the three-component velocity data using specialized software, the TFI Device Control software. With respect to the probe's horizontal axis, u denotes the longitudinal or radial downburst component (positive toward the probe's head), v is perpendicular to u and positive from right-to-left when facing the probe's head, and w represents the vertical component (positive upward) [Fig. 2(b)]. The reported manufacturer's accuracy of the probes is ± 0.5 m s^{-1} in velocity measurements and $\pm 1°$ yaw and pitch angles up to approximately 30% of turbulence intensity. Probes were oriented to face the jet touchdown position (see Fig. 2), with reliable data acquisition within a $\pm 45°$ cone around their horizontal axis. Measurements below 1 m s^{-1} were excluded due to the probes' limited accuracy at low speeds. These limitations arise from several factors: (i) Cobra probes measure velocity based on differential pressure; at low velocities, the pressure difference is minimal, resulting in a poor signal-to-noise ratio. (ii) The calibration process of Cobra probes is optimized for higher velocities; at lower speeds, the calibration curve becomes less reliable. (iii) They are designed to capture high-frequency velocity fluctuations; however, at low wind speeds, their dynamic response becomes less effective. (iv) Cobra probes rely on flow interaction with the probe head; at low wind speeds, the flow may not develop properly around the probe, leading to measurement inaccuracies. The instruments were arranged in a three-dimensional (3D) grid to ensure a good spatial resolution of the reconstructed flow field (Fig. 2). The instruments recorded data at 2500 Hz, providing excellent temporal resolution. Between 7 and 10 Cobra probes were mounted on a vertical stiff mast extending from 0.04 to 0.70 or 1.00 m above the ground level, depending on the case. The mast was subsequently placed at 10 radial positions, ranging from $r/D = 0.2$ to 2.0 with a step of 0.2, where $r/D = 0$ corresponds to the geometric location of jet touchdown on the floor. This corresponds to the geometric center of the testing chamber for all experimental cases. The radial location $r/D = 0.8$ was moved to 0.75 due to floor irregularities. Seven azimuthal locations α on the horizontal were covered, from 0° to 180° with steps 30°, where $\alpha = 0°$ aligned with the incoming ABL flow direction. Symmetry with respect to the ABL wind allowed mirroring results to the other half-plane. For vertDB, measurements were limited to $\alpha = 90°$ under the assumption of radial symmetry in the absence of ABL flow or jet-axis tilting. For each run (i.e., measurement position), ten experimental repetitions were conducted to enhance the statistical significance of the results. Unless otherwise stated, the results presented hereafter represent the ensemble average of the individual runs' outcomes. All experimental signals were synchronized based on the time of opening of the nozzle's louvers releasing the downburst jet.

Table I lists the Cobra probes' heights, geometric configurations, and dynamic parameters for each experimental case.

C. The continuous wavelet transform

This section illustrates a brief outline of the CWT. For further details, the reader is invited to see Buresti *et al.*, 2004; Mariotti, 2018; and Brusco *et al.*, 2022a.

A wavelet is any real or complex function $\psi(t) \in L^2$ that satisfies the admissibility condition

$$C_\psi = \int_{-\infty}^{\infty} \left|\hat{\psi}(\omega)\right|^2 |\omega^{-1}| d\omega < \infty, \tag{1}$$

where $\hat{\psi}(\omega)$ is the Fourier transform of $\psi(t)$. The function $\psi(t)$, known as mother wavelet, generates a family of wavelets $\psi_{a\tau}(t)$ via translation and dilation,

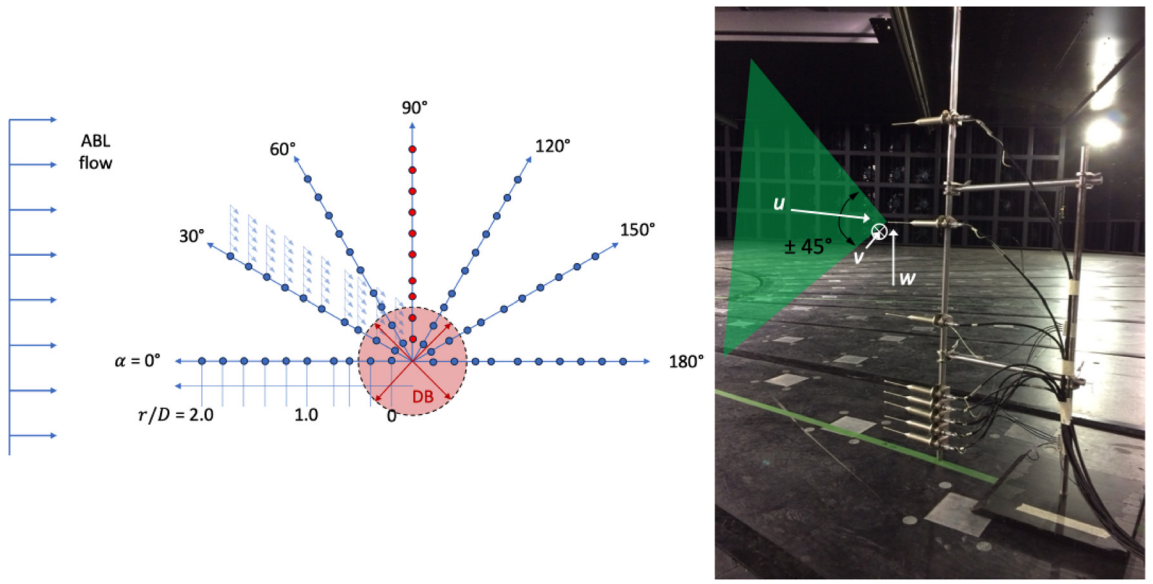

FIG. 2. (a) Schematics (top-view) of Cobra probes' setup (not-to-scale). (b) Photograph of the Cobra probes installed on the mast and schematics of the reference system.

TABLE I. Geometric and dynamic setup. Case name (Case); jet diameter (D); IJ speed (w_{IJ}); Reynolds numbers (Re); ABL speed (u_{ABL}); jet tilting angle (θ); equivalent translation velocity (V_S); equivalent full-scale roughness length ($z_{0,eq}$); radial measurement locations (r/D); azimuthal measurement locations (α); height measurement locations (z/D); and experimental repetitions (Reps.). $*$ $r/D = 0.8$ is moved to 0.75 due to irregularities of chamber floor.

Case	D (m)	w_{IJ} (m s^{-1})	$Re \times 10^6$	u_{ABL} (m s^{-1})	θ (°)	V_S (m s^{-1})	$z_{0,eq}$ (m)	r/D^* (\)	α (°)	z/D (\)	Reps.
vertDB	3.2	8.9	1.92	0	0	0	0.007	0.2:0.2:2.0	90	0.012, 0.022, 0.031, 0.047, 0.062, 0.094, 0.125, 0.156, 0.219, 0.312	10
	3.2	8.9	1.92	0	0	0	0.020	0.2:0.2:2.0	90	0.012, 0.022, 0.031, 0.047, 0.062, 0.094, 0.125, 0.156, 0.219, 0.312	10
	3.2	8.9	1.92	0	0	0	0.320	0.2:0.2:2.0	90	0.012, 0.022, 0.031, 0.047, 0.062, 0.094, 0.125, 0.156, 0.219, 0.312	10
	3.2	12.4	2.68	0	0	0	0.007	0.2:0.2:2.0	90	0.012, 0.022, 0.031, 0.047, 0.062, 0.094, 0.125, 0.156, 0.219, 0.312	10
	3.2	12.4	2.68	0	0	0	0.020	0.2:0.2:2.0	90	0.012, 0.022, 0.031, 0.047, 0.062, 0.094, 0.125, 0.156, 0.219, 0.312	10
	3.2	12.4	2.68	0	0	0	0.320	0.2:0.2:2.0	90	0.012, 0.022, 0.031, 0.047, 0.062, 0.094, 0.125, 0.156, 0.219, 0.312	10
vertDBABL	3.2	12.4	2.68	2.5	0	0	0.007	0.2:0.2:2.0	0	0.012, 0.022, 0.031, 0.039, 0.047, 0.062, 0.094, 0.125, 0.219	10
	3.2	12.4	2.68	2.5	0	0	0.007	0.2:0.2:2.0	30:30:150	0.012, 0.022, 0.031, 0.039, 0.047, 0.094, 0.156, 0.219	10
	3.2	12.4	2.68	2.5	0	0	0.007	0.2:0.2:2.0	180	0.012, 0.022, 0.031, 0.039, 0.047, 0.062, 0.094, 0.125, 0.156, 0.219, 0.312	10
	3.2	11.8	2.55	3.9	0	0	0.007	0.2:0.2:2.0	0	0.012, 0.022, 0.031, 0.039, 0.047, 0.062, 0.094, 0.125, 0.219	10
	3.2	11.8	2.55	3.9	0	0	0.007	0.2:0.2:2.0	30:30:150	0.012, 0.022, 0.031, 0.039, 0.047, 0.094, 0.156, 0.219	10
	3.2	11.8	2.55	3.9	0	0	0.007	0.2:0.2:2.0	180	0.012, 0.022, 0.031, 0.039, 0.047, 0.062, 0.094, 0.125, 0.156, 0.219, 0.312	10
inclDB	3.2	12.4	2.68	0	30	6.2	0.007	0.2:0.2:2.0	0:30:180	0.012, 0.022, 0.031, 0.039, 0.047, 0.062, 0.094, 0.125, 0.156, 0.219	10
inclDBABL	3.2	11.8	2.55	3.9	30	5.9	0.007	0.2:0.2:2.0	0	0.012, 0.022, 0.031, 0.039, 0.047, 0.062, 0.094, 0.125, 0.219, 0.281	10
	3.2	11.8	2.55	3.9	30	5.9	0.007	0.2:0.2:2.0	30:30:150	0.012, 0.022, 0.031, 0.039, 0.047, 0.062, 0.094, 0.125, 0.156, 0.219	10
	3.2	11.8	2.55	3.9	30	5.9	0.007	0.2:0.2:2.0	180	0.012, 0.022, 0.031, 0.039, 0.047, 0.062, 0.094, 0.125, 0.156, 0.219, 0.312	10

$$\psi_{a\tau}(t) = a^{-\frac{1}{p}}\psi\left(\frac{t-\tau}{a}\right), \tag{2}$$

where a is the scale (dilation), τ is the translation, and p determines the normalization. Specifically, setting $p = 1$ or 2 ensures that the L^1 or L^2 norm of $\psi_{a\tau}(t)$ remains constant and equal to that of the mother wavelet. The dilation in Eq. (2) ensures that all wavelet functions retain the same number of oscillations, enabling better frequency resolution at low frequencies and better time resolution at high frequencies.

The CWT of a function $x(t)$ is the L^2 inner product between $x(t)$ and the wavelet family $\psi_{a\tau}(t)$,

$$W_x(a,\tau) = \int_{-\infty}^{\infty} x(t)\psi^*_{a\tau}(t)dt, \tag{3}$$

where * denotes complex conjugation. The inverse transform returns the signal in the time domain

$$x(t) = \frac{1}{C_\psi}\int_{-\infty}^{\infty}\int_{0}^{\infty} a^{\left(\frac{2}{p}-3\right)} W_x(a,\tau)\psi_{a\tau}(t)dad\tau. \tag{4}$$

The energy of the signal can be recovered from the wavelet transform as

$$\|x(t)\|^2 = \frac{1}{C_\psi}\int_{0}^{\infty}\int_{-\infty}^{\infty} a^{\left(\frac{2}{p}-3\right)}\left|W_x(a,\tau)\right|^2 dad\tau. \tag{5}$$

L^1 is used in our study to characterize with accuracy the lower frequency content of the signal where most of the energy is retained.

Concerning the mother wavelet, the complex Morlet wavelet is used in our work,

$$\psi(t) = e^{i\omega_0 t}e^{-t^2/2}, \tag{6}$$

with Fourier transform,

$$\hat{\psi}(\omega) = e^{-(\omega-\omega_0)^2/2}. \tag{7}$$

Although the Morlet wavelet does not strictly satisfy the admissibility condition, it becomes admissible for $\omega_0 \geq 6$, which is sufficient for practical purposes. The Morlet wavelet is chosen for its favorable properties, including a simple relationship between the scale a and Fourier frequency f, $f = \omega_0/(2\pi a)$. Its optimal time-frequency concentration provides an excellent compromise between time and frequency resolution (Brusco *et al.*, 2022a). For applications requiring a higher-frequency resolution, the Morlet wavelet's resolution can be adjusted by increasing the central frequency parameter, ω_0, at the cost of reduced time resolution. When a complex wavelet is used, the transform output is complex and is often visualized through maps where the square modulus of the transform, directly linked to the signal's energy, is reported. The wavelet transform output at specific time-frequency pairs represents the contribution of the signal's energy in corresponding neighbors of time and frequency.

The CWT may also conveniently be used to characterize the correlation between two signals, providing the time variation of the frequencies simultaneously present in the two signals that contribute to their correlation, as well as the phase between the fluctuations at those frequencies (e.g., Brusco *et al.*, 2023). The cross product between the wavelet transforms W_x and W_y of two different signals $x(t)$ and $y(t)$ is the wavelet cross-scalogram, $W_{xy}(a,\tau)$, which may be evaluated as

$$W_{xy}(a,\tau) = W_x(a,\tau)\cdot W_y^*(a,\tau). \tag{8}$$

We may then introduce a wavelet local correlation coefficient (Buresti *et al.*, 2004),

$$WLCC_{xy}(a,\tau) = \frac{\mathrm{Re}\left(W_{xy}(a,\tau)\right)}{\left|W_x(a,\tau)\right|\cdot\left|W_y(a,\tau)\right|}, \tag{9}$$

where $\mathrm{Re}(W_{xy}(a,\tau))$ indicates the real part of W_{xy}. The phase angle between the two signals will be the result of

$$\theta_{xy}(a,\tau) = \frac{\mathrm{Im}\left(W_{xy}(a,\tau)\right)}{\mathrm{Re}(W_{xy})(a,\tau),} \tag{10}$$

where $\mathrm{Im}(W_{xy}(a,\tau))$ represents the imaginary part of W_{xy}.

III. RESULTS AND DISCUSSION

A. Time-frequency energy maps

The wavelet maps in Figs. 3–6 reveal the energy content—evaluated as the square modulus map of the wavelet transform—of the experimental downburst signals, serving as a crucial tool for interpreting the underlying physics of the downburst outflow and its spatiotemporal evolution. The wavelet maps below are shown at $z/D = 0.031$, which corresponds to the average position of maximum velocity across all cases and is used for consistency in their representation. The reader can refer to the sketch in Fig. 2(a) to visualize the corresponding radial and azimuth measurement locations. These maps consistently exhibit high-energy levels at very low frequencies throughout the time period. This elevated energy content does not have a physical meaning, being associated with the length of the time signal. At slightly higher frequencies, a secondary region of elevated energy extends throughout the duration of the downburst signal. This phenomenon is attributed to the background outflow being radially "pulled" outward by the propagating vortex structures. The remaining energy content emphasizes the dynamics of the PV and other vortex structures, which are inherently reflected in the mean and turbulent components of the velocity signals. These components are depicted in the top graphs as wind speed time series, represented by the red and black lines, respectively. Canepa *et al.* (2022c) identified three distinct stages in the reproduced downburst signals, consistent with observations in full-scale cases: (1) velocity ramp-up and PV, associated with the PV approaching and passing over the measuring instrument; (2) a velocity plateau, corresponding to the PV moving away while the instrument records the subsequent trailing vortices (TVs); and (3) velocity dissipation, linked to the closure of the bell mouth louvers and the decay of velocity.

The vertDB case (Fig. 3) exhibits similar characteristics across the three surface roughness configurations. The energy associated with the passage of the primary vortex (PV) consistently appears within the 0.5–1.5 Hz frequency band, aligning with the observations of Canepa *et al.* (2022b). Based on a vortex diameter of approximately 0.70–0.80 m, as reported by Junayed *et al.* (2019) from experiments at the WindEEE Dome and supported by the numerical simulations of Žužul *et al.* (2024), the PV propagation velocity (U_{PV}) can be approximated using the relation $U_{PV} = f_{PV}\cdot\lambda$. Here, f_{PV} is the frequency of maximum energy content associated with the PV, and λ, approximated as the PV diameter, serves as a representative wavelength. This yields a propagation velocity (U_{PV}) between 0.35 and 1.20 m s^{-1}. At

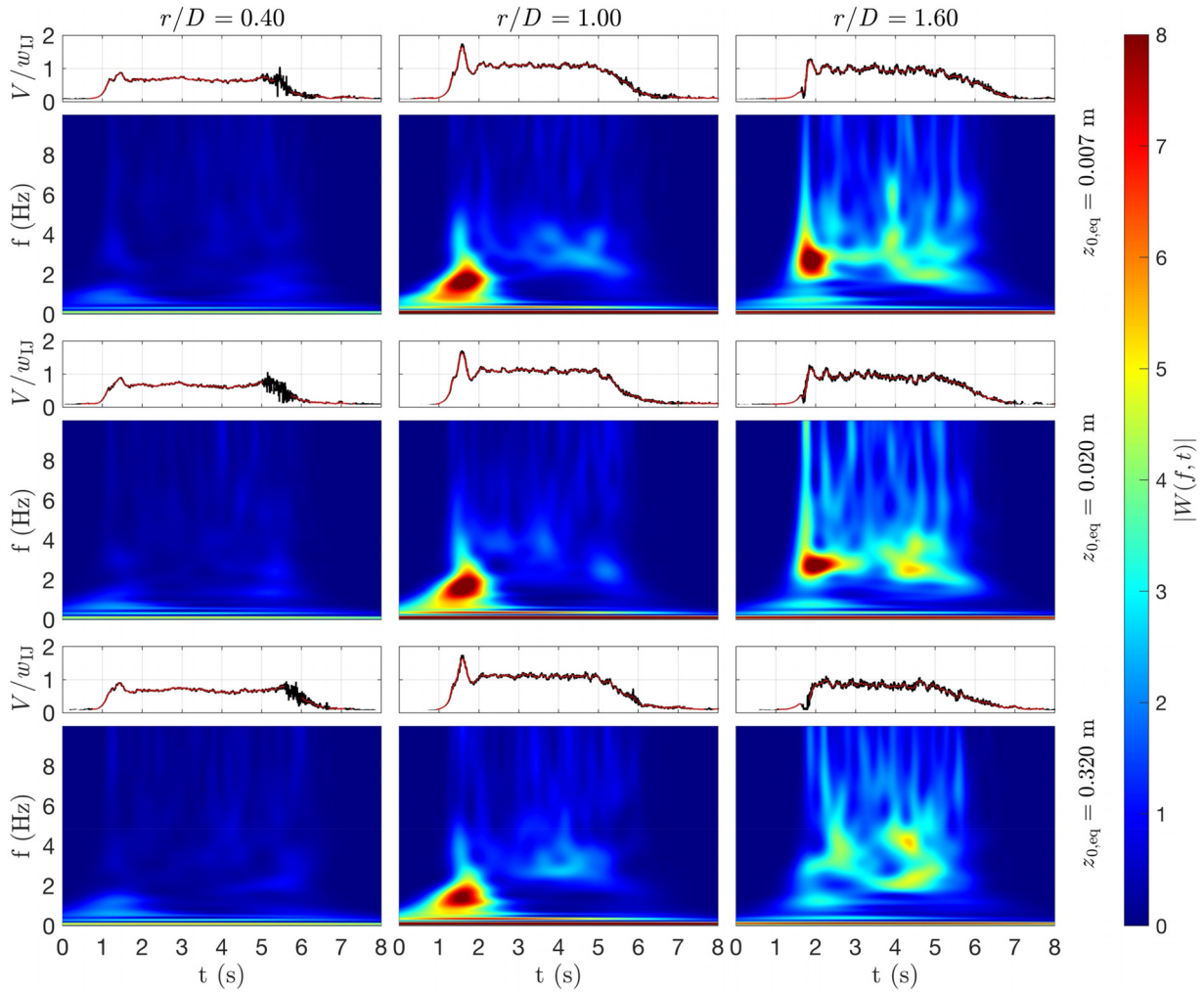

FIG. 3. Ensemble mean of experimental repetitions at $z/D = 0.031$, various radial positions (columns) and different roughness lengths (rows) for the vertDB case ($\mathrm{Re} = 2.68 \times 10^6$): time series of the instantaneous (black line) and slowly varying mean (red line) velocity magnitude, computed as the linear combination of three velocity components (u, v, and w) (top graphs), and corresponding energy content in the form of wavelet maps (bottom graphs).

$r/D = 1.0$, the PV energy content becomes intermixed with higher energy contributions at larger frequencies (up to 2.5–3 Hz) due to increased turbulence from the boundary layer detachment near the surface. This interaction leads to the formation of a counter-rotating vortex structure (secondary vortex, SV) ahead of the PV, manifested as a small bump during the wind speed ramp-up. The interaction between the PV and SV enhances turbulence levels in the flow. At $r/D = 1.6$, the SV is fully developed (Canepa *et al.*, 2022b), and the separation between the PV and SV becomes evident in both the wind speed time series—where a short increase in wind speed now precedes the main ramp-up—and the energy maps. At this location, the SV contributes to frequencies exceeding 3 Hz. Following the passage of the PV and SV, high-energy content develops due to the appearance of trailing vortices (TVs), which are observed at higher frequencies and, therefore, propagate faster than the PV.

The inclusion of the ABL flow in the vertDBABL case (Fig. 4) disrupts the radial symmetry of the downburst (DB) outflow at the ground. Consequently, the flow field is experimentally characterized at different azimuthal (α) as well as radial (r) locations. For better representativeness in understanding the physical interaction between the downburst and the ABL flow, the position $r/D = 0.6$ is depicted instead of $r/D = 0.4$: At $\alpha = 0°$, where the DB and ABL collide head-on, this interaction does not occur near the jet touchdown point ($r/D = 0.4$); conversely, at $\alpha = 180°$, where the DB and ABL propagate in the same direction, the ABL deflects the descending IJ, causing the outflow to shift toward larger radial locations. Here, $r/D = 0.4$ lies even closer to the IJ touchdown point, making the analysis of the flow field less meaningful, whilst $r/D = 0.6$ still falls within the jet's ground projection (Canepa *et al.*, 2022a). The interaction between the DB and ABL at $\alpha = 0°$ begins approximately at $r/D = 0.6$, producing elevated energy levels in the flow field. The velocity peak is characterized by significant energy content in the 0.5–5 Hz frequency band, driven by the entrainment of ABL flow into the PV circulation. This interaction accelerates the flow field

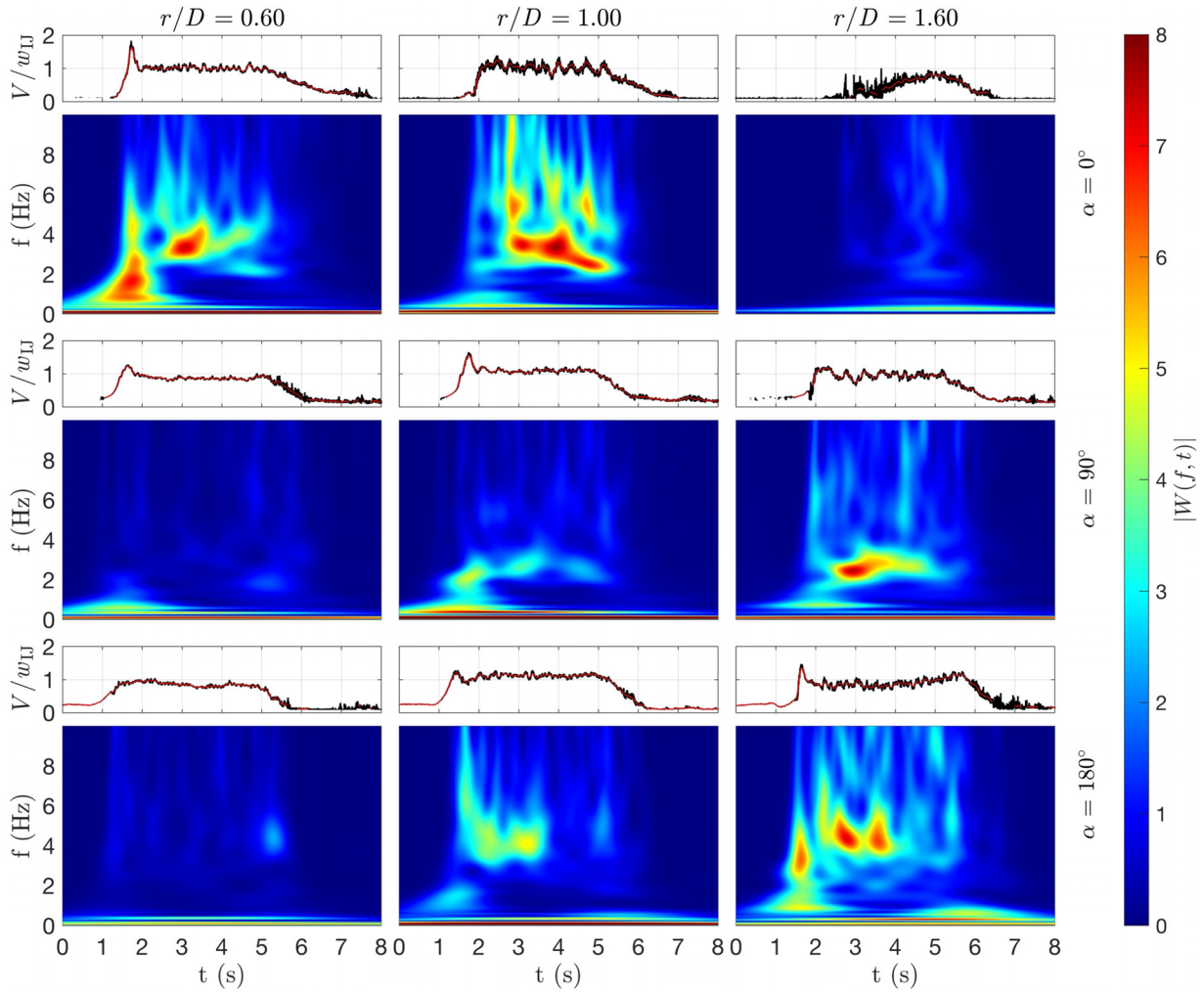

FIG. 4. Same as Fig. 3 but for the vertDBABL case (larger ABL fan speed). Rows show different azimuthal positions.

(Canepa *et al.*, 2022a) and, along with the increased turbulence caused by the flow interplay, broadens the frequency band associated with the PV passage. Despite being hindered by the counter-directed ABL, the PV propagates up to $r/D = 1.0$, where the stronger ABL forces it into a "stagnation" regime. At this location, the PV's contribution to the signal energy becomes more distinct and separated from the higher-frequency energy, primarily arising from the approaching TVs, which may also be partially embedded within the PV structure. The PV and DB outflow do not reach $r/D = 1.6$, where the velocity signal energy is negligible. At $\alpha = 90°$, perpendicular to the ABL's outgoing direction and its frontal interaction with the DB, the azimuthal location is minimally affected by the asymmetry in the flow field. Consequently, the PV and SV produce distinct contributions to the wavelet maps, as do the subsequent TVs. Similar observations can be made at $\alpha = 180°$, although the turbulence intensity is higher due to the alignment of the DB and ABL in the same direction, leading to increased energy levels in the wind speed signal. The energy content at lower frequencies toward the end of the wind speed time series is unrelated to physical flow properties and instead arises from the closure mechanism of the bell mouth louvers.

The inclination of the jet axis toward the side opposite the 60-fan wall (Fig. 5) results in a weaker downburst outflow and a less pronounced PV at $\alpha = 0°$. Particularly, the PV structure appears less defined, with increased turbulence levels contributing to higher-frequency energy content at $r/D = 1.0$. At $\alpha = 90°$, the flow remains relatively unaffected by the asymmetries introduced by the jet-axis inclination, and the contribution of the PV at $r/D = 1.0$ is well defined, while its interaction with SV at $r/D = 1.6$ provides a clear distinction between their respective contributions. Conversely, the increased intensity of the outflow on the front-wind side ($\alpha = 180°$) generates significant energy levels in the signal, associated with vortex structures (PV, SV, and TVs). These structures are particularly well defined and distinct at $r/D = 1.6$, reflecting the stronger and more organized dynamics of the flow at this azimuthal location.

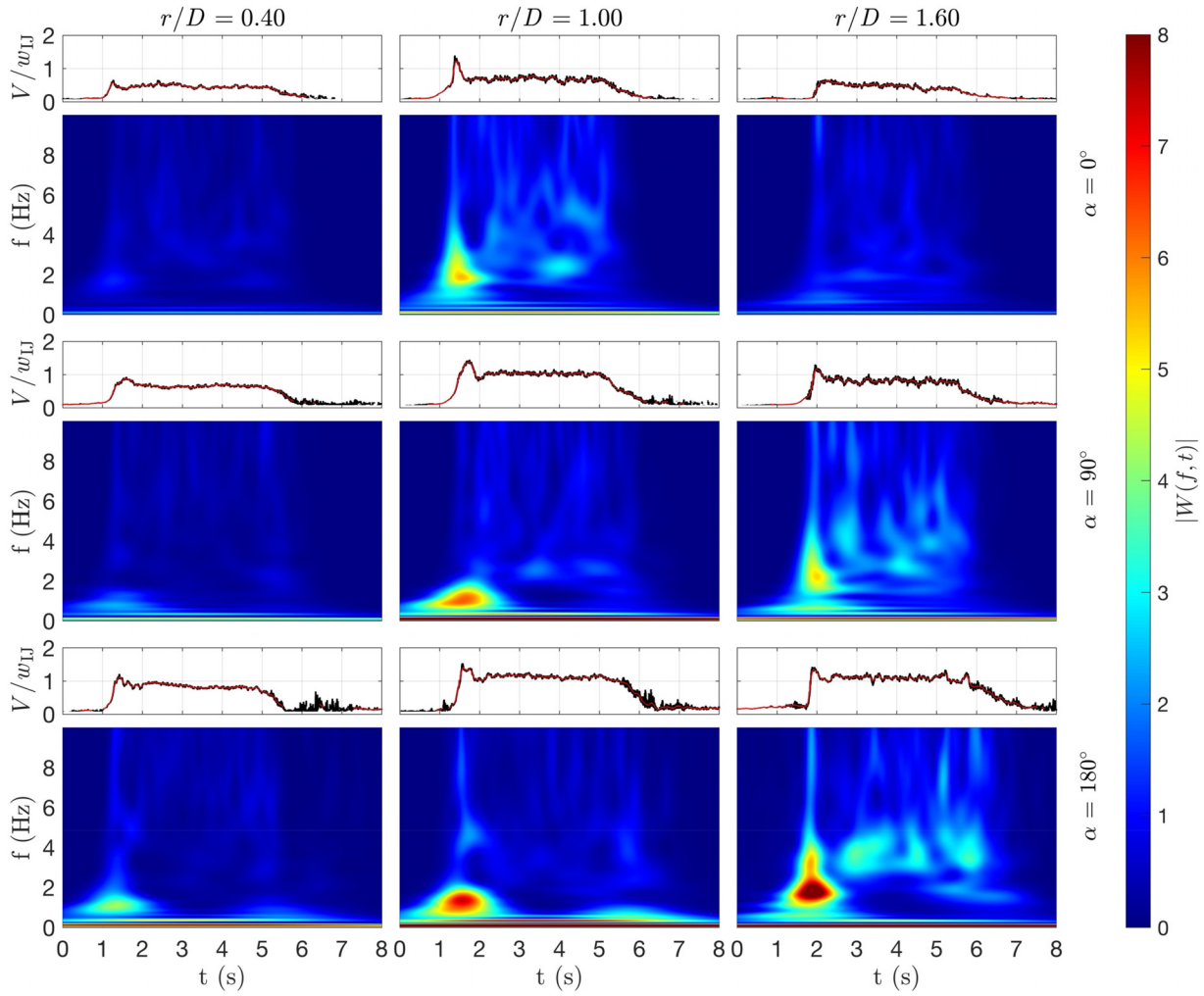

FIG. 5. Same as Fig. 3 but for the inclDB case. Rows show different azimuthal positions.

The inclusion of the ABL flow in the inclined DB configuration (Fig. 6) generally weakens the downburst but enhances the distinction between the energy contributions of PV and SV.

B. Frequency-based reconstruction of velocity time series

This section presents the application of the inverse wavelet transform [Eq. (4)] to the previously defined wavelet maps to reconstruct the velocity time series. Specifically, the energy content is segmented into frequency bands, and Eq. (4) is then applied to each band to extract the velocity signal corresponding to the relevant band of energy. For brevity and relevance, the analysis is limited to the case of vertDB007 ($Re = 1.92 \times 10^6$) at radial locations $r/D = 1.0$ and 1.6, and $z/D = 0.031$.

Figure 7 provides a schematic representation of the flow dynamics at these radial locations alongside the corresponding velocity recordings from the Cobra probe. At $r/D = 1.0$, which corresponds to the position of the overall maximum velocity (Canepa *et al.*, 2022b), the PV has just impacted the ground, and the radially propagating motion has not yet developed. The maximum velocity [red box in Fig. 7(c)], occurring between the lower end of the vortex and the ground, can be attributed solely to the vorticity of the PV [red circle in Fig. 7(a)]. The subsequent TVs [yellow circles in Fig. 7(a)] are observed in the velocity signal as local weak peaks [yellow box in Fig. 7(c)]. At $r/D = 1.6$, the PV detaches from the surface, causing a separation of the boundary layer flow beneath its structure. The counter-rotating recirculation zone (SV) [green circle in Fig. 7(b)], located ahead of the PV, is recorded in the velocity signal just before the main velocity peak [green box in Fig. 7(d)]. At this point, the maximum velocity arises from the interaction between the PV and SV and is particularly pronounced at the interface between these two vortices, accompanied by a significant vertically upward flow component.

Figure 8 illustrates the application of Eq. (4) to various frequency bands comprising the velocity signal at $r/D = 1.0$ and 1.6. The analysis focuses on the frequency range between 0 and 5 Hz, which

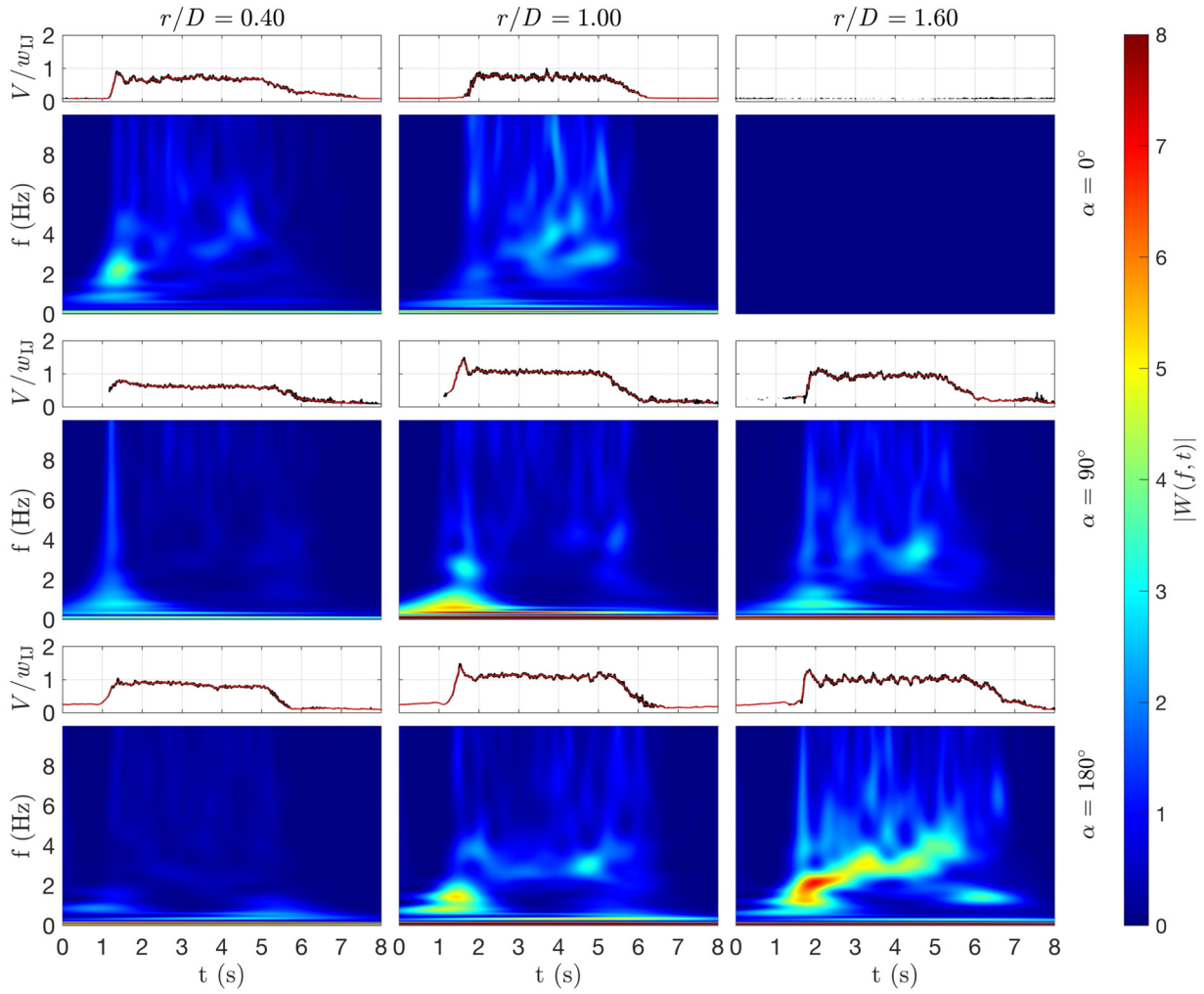

FIG. 6. Same as Fig. 3 but for the inclDBABL case. Rows show different azimuthal positions.

encapsulates almost the entirety of the harmonic content of the time-domain signal. This range is arbitrarily divided into four frequency bands Δf: 0–0.5 Hz [Figs. 8(a) and 8(f)], 0.5–1.5 Hz [Figs. 8(b) and 8(g)], 1.5–2.5 Hz [Figs. 8(c) and 8(h)], and 2.5–5 Hz [Figs. 8(d) and 8(i)]. They are labeled in the legend as "WF—lower bound—higher bound." The reconstructed signals for all bands are superimposed in Figs. 8(e) and 8(j).

The harmonic content at the very low frequencies [Figs. 8(a) and 8(f)] represents the background outflow velocity, which remains relatively constant throughout the duration of the downburst. As discussed previously, this component corresponds to the flow being pulled outward by the propagating vortical structures. The frequency band $\Delta f = 0.5$–1.5 Hz [Figs. 8(b) and 8(g)] captures the contribution of the vortices' advection to the velocity recorded by the probe. This contribution is most significant during the passage of the PV—causing the maximum velocity to prominently emerge from the background outflow velocity. However, the TVs also manifest clearly within this frequency band's energy content. Two noteworthy observations arise from this analysis: first, the negative velocity values in the reconstructed signals likely indicate the backward flow component associated with the vortices. Second, a slight delay is observed between the maximum reconstructed signal and the maximum wind speed at $r/D = 1.6$. This delay occurs because the instrument initially detects the interaction between the PV and the SV, which defines the overall maximum velocity, followed shortly after by the passage of the PV itself over the instrument. The frequency band $\Delta f = 1.5$–2.5 Hz corresponds to the vorticity contribution, which is notably higher at $r/D = 1.6$, where the development of the PV and subsequent TVs is fully developed. The boundary layer detachment and PV–SV interaction contribute to the higher signal energy compared to $r/D = 1.0$. As it is well known and intrinsic to the decomposition of velocity signals into mean and fluctuating components, turbulent fluctuations dominate the higher frequencies of the energy spectrum. At $r/D = 1.0$, the wind speed signal is primarily governed by the organized and coherent vortex structures, which contribute to the mean component of the velocity. In contrast, at $r/D = 1.6$, the turbulence level rises

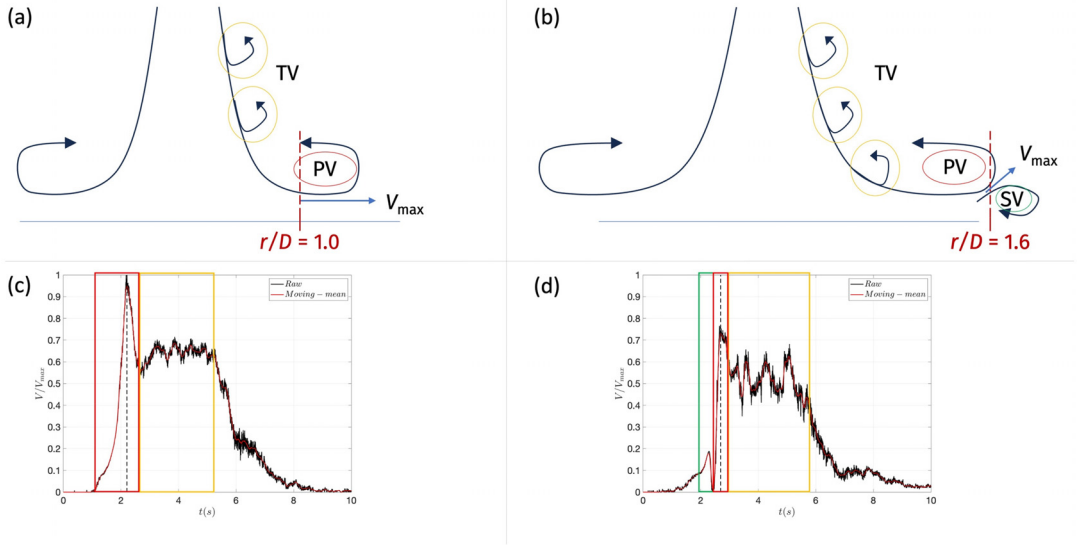

FIG. 7. Schematics of flow field (vertical view) for the case vertDB at $r/D = 1.0$ (a) and 1.6 (b), and corresponding wind speed stages from Cobra probe recordings (c) and (d).

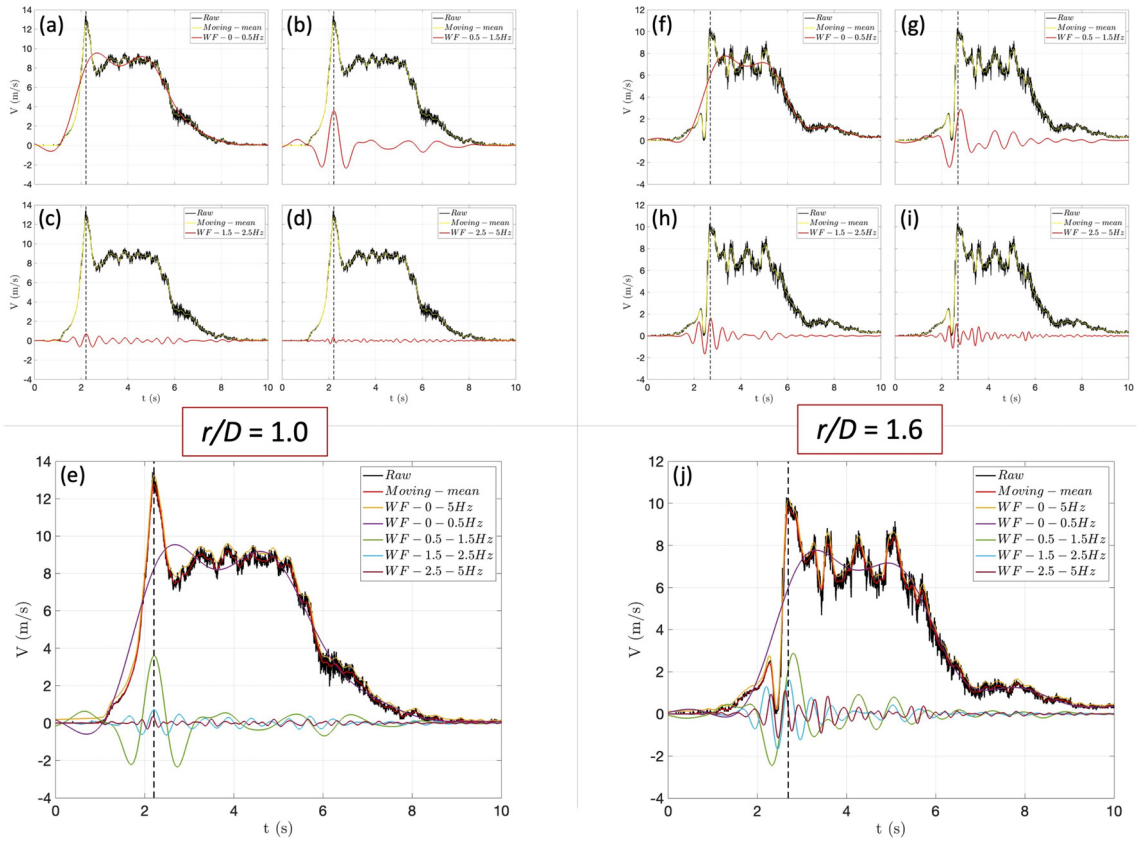

FIG. 8. Frequency-based reconstruction of wind speed time series for the case vertDB at $r/D = 1.0$ (a)–(e) and 1.6 (f)–(j). Panels (a)–(d) and (f)–(i) illustrate the reconstruction divided into individual frequency bands, while panels (e) and (j) present the superposition of all considered frequency bands.

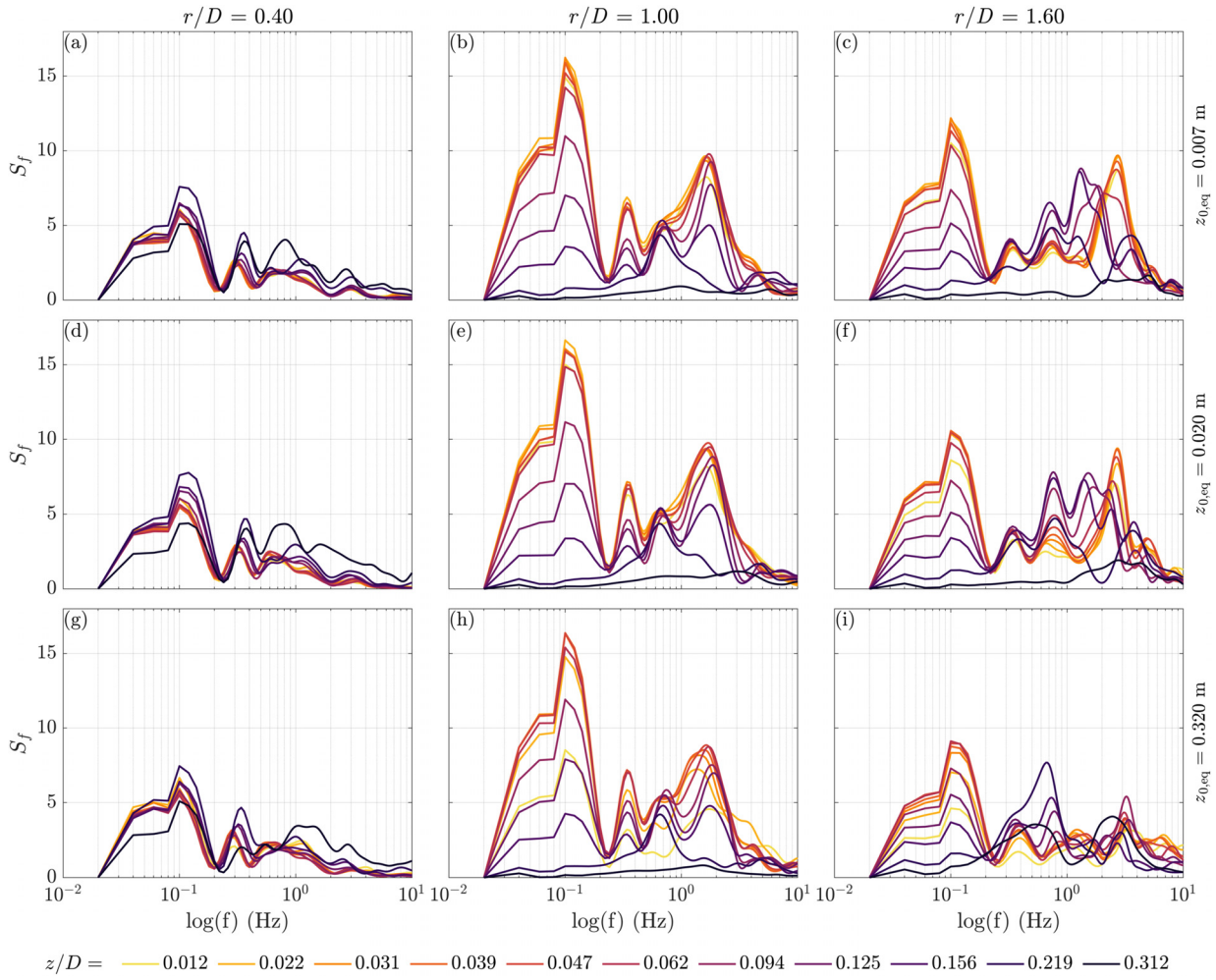

FIG. 9. Wavelet spectra for the vertDB case across all measurement heights at the time of maximum wind speed recorded at $z/D = 0.012$. The columns represent different radial locations: $r/D = 0.4$ [(a), (d), and (g)], 1.0 [(b), (e), and (h)], and 1.6 [(c), (f), and (i)]. The rows correspond to the three different roughness lengths tested: $z_{0,eq} = 0.007$ m (a)–(c), 0.020 m (d)–(f), and 0.320 m (g)–(i).

significantly as the flow loses its organized structure, dispersing into a more three-dimensional pattern. This transition allows for increased entrainment of ambient air, enhancing flow mixing and, consequently, the magnitude of turbulent fluctuations at high frequencies above 2.5 Hz.

C. Along-height evolution of PV energy content

Figures 9–12 present a detailed spectral analysis of the wavelet signals across all measurement heights. This analysis focuses on the time of maximum wind speed occurrence at the lowest measurement height, which serves as the reference signal, being located below the lower end of the PV. The graphs below effectively represent cross sections at the moment of the wavelet maps' maximum values, as shown in Figs. 3–6. A common feature among these figures is the consistent emergence of an energy peak around the frequency $f = 0.1$ Hz. This peak is attributed to the energy of the downburst-related component of the wind speed signal, and is linked to the temporal length of the signal. Alongside this peak, a smaller secondary peak below 0.5 Hz reflects the background wind speed during the event. This background flow represents the wind not directly encapsulated within the propagating vortex structures but rather occurring in the regions between them. For frequencies above 0.5 Hz, the influence of propagating vortices becomes evident, appearing in a bimodal distribution that we speculate arises from the distinct contributions of vorticity and advection components within the vortex. For frequencies between 0.5 and 1 Hz, the vortex advection dominates the energy spectra, producing a consistent local peak across measurement heights. However, the energy magnitudes vary notably depending on the reference height. At $r/D = 0.4$, within the projected area of the vertical jet on the ground, the maximum intensities are attributed to the PV and subsequent TVs at higher heights. At these heights, the flow—and the embedded vortices—are deflected from a vertical to a horizontal orientation due to the pressure gradient (Canepa *et al.*, 2022b). This deflection accelerates the TVs,

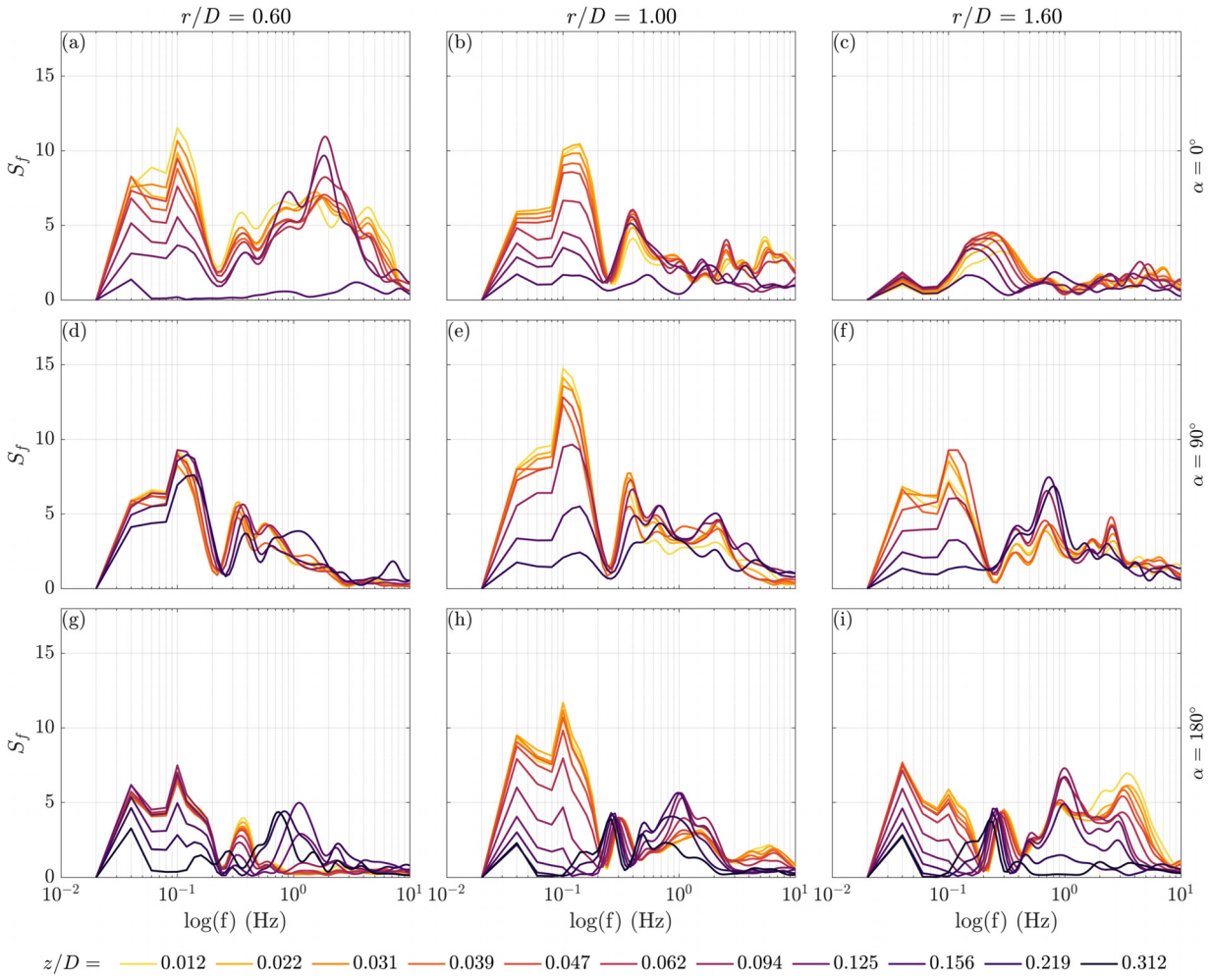

FIG. 10. Same as Fig. 9 but for the case vertDBABL. Rows show different azimuthal positions: $\alpha = 0°$ (a)–(c), 90° (d)–(f), and 180° (g)–(i).

which are therefore observed at slightly higher frequencies. At $r/D = 1.0$, the advection of vortices contributes relatively uniformly to the energy spectra in terms of both magnitude and frequency. Conversely, at $r/D = 1.6$, the formation of the secondary vortex (SV) and the detachment of the boundary layer elevate the PV, with the dominant energy peak occurring higher above the ground. This phenomenon is particularly evident in the highest roughness case (vertDB320), where the top measurement height exhibits a pronounced energy peak at lower frequencies compared to lower heights. Here, the interaction of the SV with the rough surface increases turbulence, shifting the energy spectrum toward higher frequencies. For frequencies above 1 Hz, the energy spectrum is dominated by the vorticity of traveling vortices. At $r/D = 0.4$, where the recreated downburst is primarily influenced by the vertical advection of vortices, this contribution is minimal. In contrast, at $r/D = 1.0$, higher energy levels are observed at the lower measurement heights. At higher elevations, the entrainment of ambient air into the vortex structure weakens the energy while increasing turbulence and, consequently, the frequency of occurrence. At $r/D = 1.6$, a clear separation is evident between the energy peaks associated with lower and higher measurement heights. This separation is linked to the formation of the SV. At lower heights, the friction between the PV and the SV increases energy and turbulence, shifting the spectrum to higher frequencies. In contrast, the Cobra probes at higher installation heights predominantly capture the PV, with less turbulence and lower energy levels. Smaller subsequent peaks in the spectra correspond to the onset and passage of smaller TVs.

The enhanced contribution of vorticity above 1 Hz for $\alpha = 0°$ and $r/D = 0.6$ is evident in Fig. 10(a). Canepa *et al.* (2022a) demonstrated that the frontal collision between the downburst PV and the counter-directed ABL flow results in two key effects. First, the PV is slowed down and stagnates above the same radial location as long as both flows are sustained by their respective fans. Second, the matching direction of relative vorticity between the PV and the ABL at this location causes the upper ABL air to become entrained into the rotating PV structure. This interaction enhances the PV vorticity and increases the associated horizontal flow beneath the vortex structure, which is prominently reflected

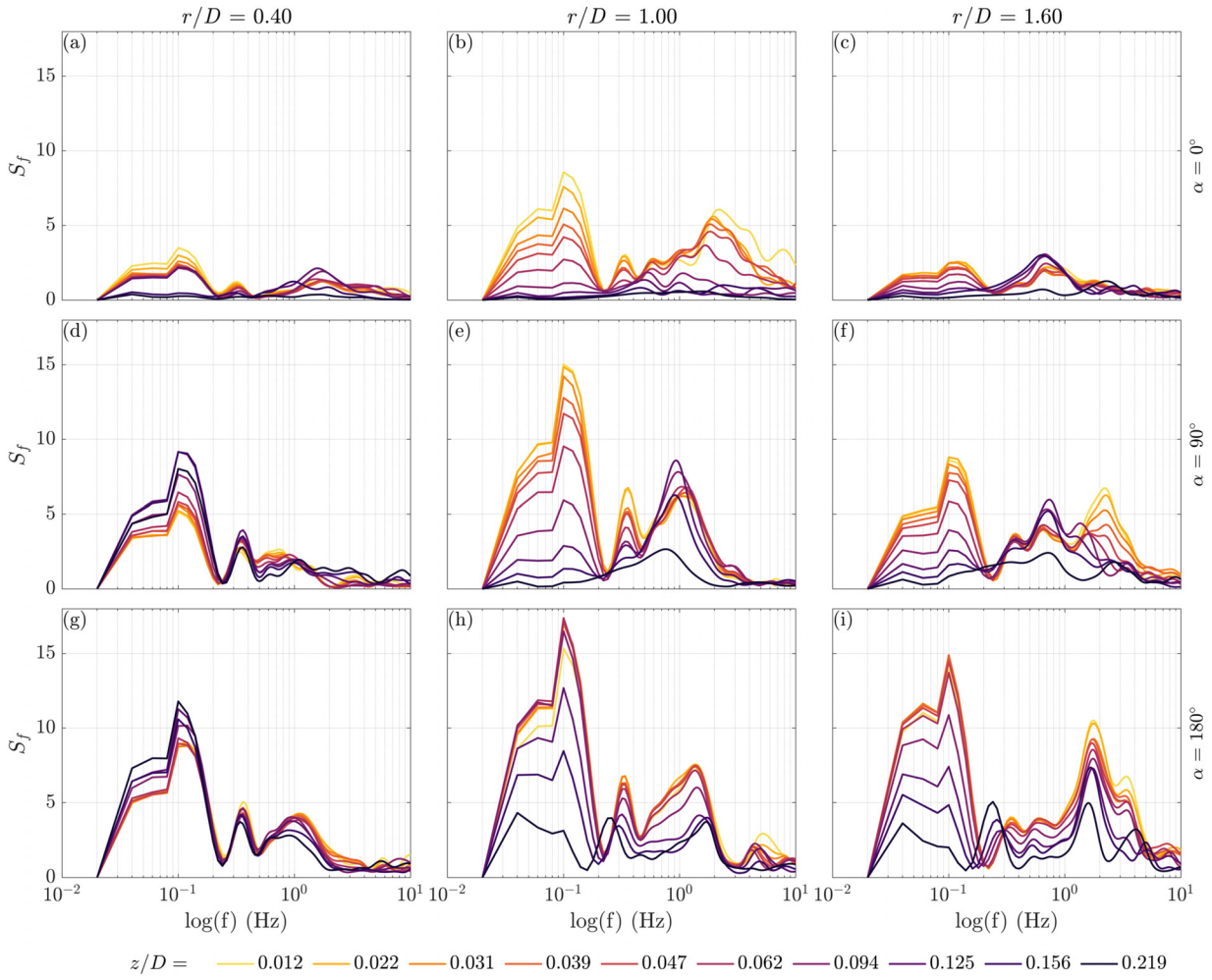

FIG. 11. Same as Fig. 9 but for the case inclDB. Rows show different azimuthal positions: $\alpha = 0°$ (a)–(c), 90° (d)–(f), and 180° (g)–(i).

in the energy spectrum. At farther radial locations for $\alpha = 0°$, the recorded energy is low—except at very low frequencies corresponding to the overall downburst duration. This reduction occurs because the downburst outflow and PV are blocked closer to the jet touchdown point. At $\alpha = 90°$, a location expected to be less influenced by the asymmetry introduced by the ABL flow, the vorticity contribution appears partially filtered out compared to the vertDB case. At $\alpha = 180°$, vortex advection and vorticity again contribute significantly to the energy, particularly at $r/D = 1.6$, with higher energy observed at greater heights and lower energy at reduced heights.

The inclDB case exhibits very low energy content at $\alpha = 0°$. The inclination of the jet axis at the ground toward $\alpha = 180°$ generates a flow speed-up effect on the front-wind side ($\alpha = 90°$–$180°$) while causing a reduction in magnitude on the rear-wind side ($\alpha = 0°$–$90°$). Additionally, the louver opening direction imparts extra horizontal momentum to the downburst outflow at $\alpha = 0°$ (Canepa *et al.*, 2023), resulting in increased vorticity at $r/D = 1.0$. At $\alpha = 180°$, the inclined jet introduces additional vertical momentum into the outgoing horizontal flow, which enhances the energy level at lower heights, primarily due to advection velocity at $r/D = 1.0$. Over radial distance, as the advection term continues to increase, the vorticity contribution also becomes significant, further influencing the energy spectra.

When the ABL flow is aligned with the jet-axis inclination (toward $\alpha = 180°$), the overall intensity of the downburst diminishes at $\alpha = 0°$. At $\alpha = 180°$, the increased flow speed causes the advection and vorticity components to become intermingled and less distinguishable.

D. Insights into PV dimension

The application of Eqs. (9) and (10) to time-frequency wavelet signals recorded simultaneously at two different heights provides valuable qualitative and quantitative insights into the dimensions of the main downburst vortices, with a particular focus on the PV. The signal at $z/D = 0.012$ is used as the reference, as this height is close to the ground and consistently below the lower end of the

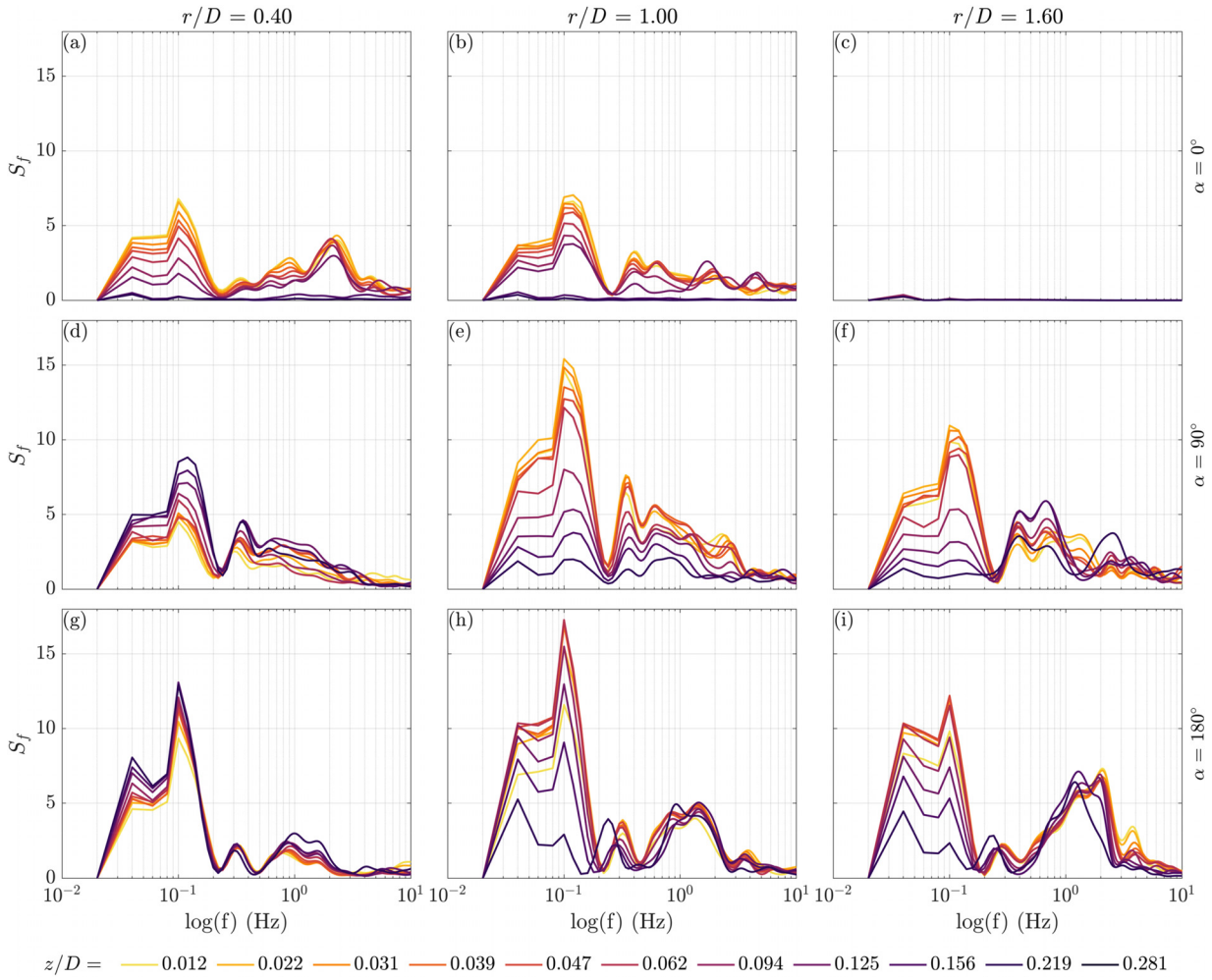

FIG. 12. Same as Fig. 9 but for the case inclDBABL. Rows show different azimuthal positions: $\alpha = 0°$ (a)–(c), 90° (d)–(f), and 180° (g)–(i).

vortex. At this height, the flow direction primarily aligns with the main outward propagation of the vortices and the overall downburst outflow.

At $r/D = 1.0$ (Fig. 13) and for the vertDB case [panels (a) and (c)], signals from heights above $z/D = 0.1$ begin to show a loss of correlation with the reference signal. However, it is only at the top measurement height ($z/D = 0.312$) that the phase angle θ undergoes a shift of nearly 180° for lower frequencies, slightly above 1 Hz. This frequency range corresponds to the passage of the PV over the measuring instrument. The 180° phase shift indicates a flow reversal, signifying that this location is above the vortex's upper end, where the flow circulates opposite to the direction beneath the vortex's lower end [see schematics in Figs. 7(a) and 7(b)]. In the vertDBABL case [Figs. 13(b) and 13(d)], the inclusion of the ABL flow enlarges the PV at the interface between the downburst and ABL, as described by Canepa *et al.* (2022a). Consequently, a flow reversal is not observed, and the phase angle remains consistent with the reference height. However, the top measurement height $z/D = 0.312$ was not recorded for this case at this specific location. For the inclDB case [Figs. 13(e) and 13(g)], the jet-axis inclination toward $\alpha = 180°$ and the additional horizontal momentum imparted by the louver's rotation during opening cause the PV to contract near the ground at $\alpha = 0°$. As a result, a phase angle shift of approximately 180° is observed at heights around $z/D = 0.22$. The embedment of the ABL flow [Figs. 13(f) and 13(h)] into the vortex structure again enlarges the size of the PV. This prevents a complete flow reversal, at least up to the top measurement height of $z/D = 0.312$.

At a greater radial distance from the jet touchdown (Fig. 14), the inclusion of the ABL flow causes the PV at $r/D = 1.6$ to lose its structure and dissipate into a highly chaotic and turbulent flow. In the vertDB case, the PV is observed to contract in size. The jet-axis inclination weakens the outflow at $\alpha = 0°$, resulting in the PV dispersing into a larger and more turbulent vortex.

IV. CONCLUSIONS AND PROSPECTS

This paper presents a novel technique for analyzing the temporal evolution of frequency content associated with non-stationary wind signals and the physical structures governing the flow field. An

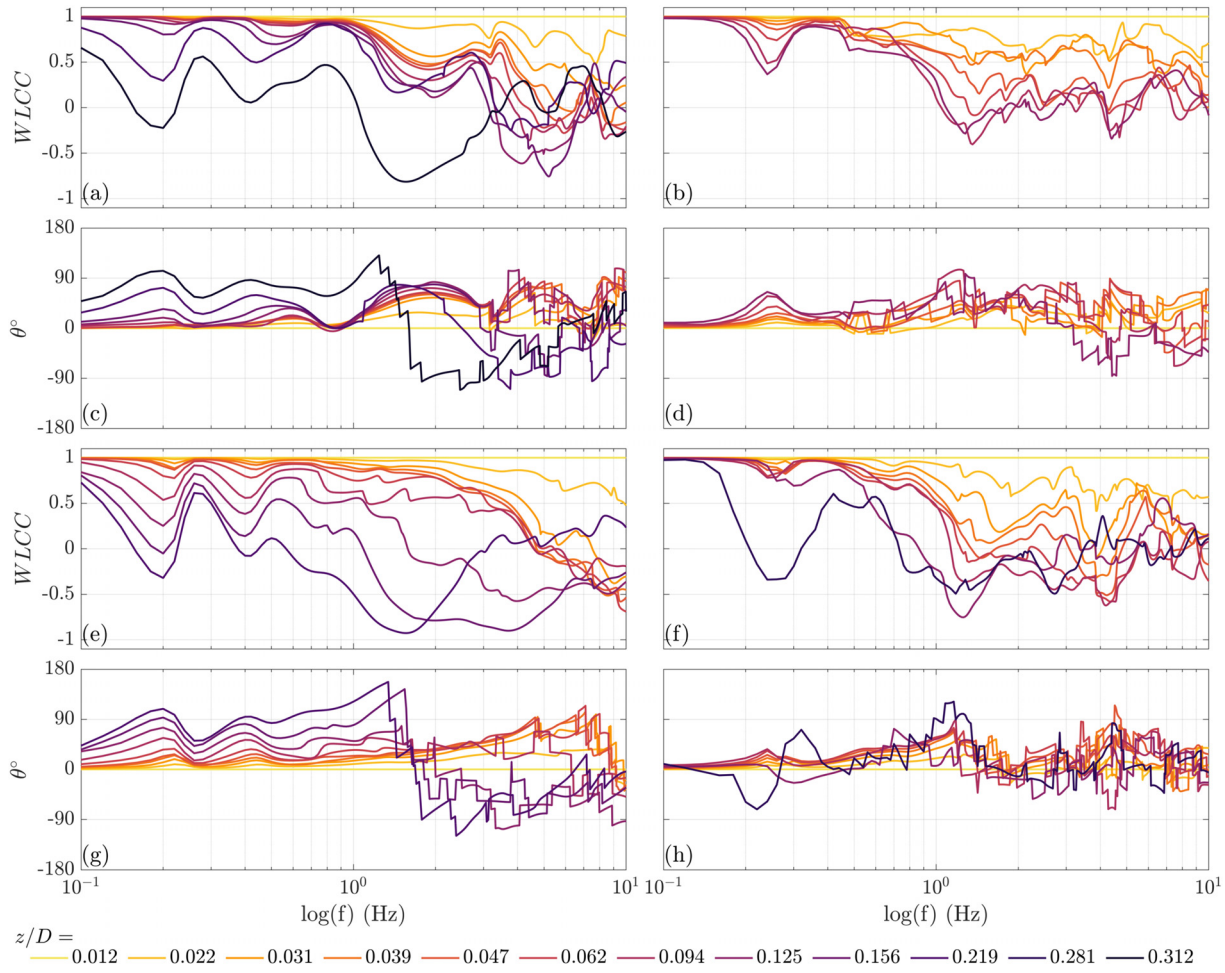

FIG. 13. Cross-correlation, WLCC [(a), (b), (e), and (f)], and phase angle, θ [(c), (d), (g), and (h)], between signals acquired at different heights and the reference height $z/D = 0.012$, at $r/D = 1.0$ for all experimental cases: vertDB ($z_{0,eq} = 0.007$ m) (a) and (c); vertDBABL ($\alpha = 0°$) (b) and (d); inclDB ($\alpha = 0°$) (e) and (g); and inclDBABL ($\alpha = 0°$) (f) and (h).

extensive experimental database of reproduced downburst winds, recorded at large geometric scales at the WindEEE Dome laboratory at Western University, Canada, was treated by means of the continuous wavelet transform (CWT) analysis. The focus of this study is on the leading vortex structures, particularly the primary vortex (PV), which is responsible for the maximum horizontal velocity near the ground and poses significant hazards to both natural and built environments.

Various downburst scenarios were analyzed and compared, including the reproduction of a vertically isolated downburst and its interaction with a developed background horizontal flow, as well as the effects of thunderstorm cloud translation. The impact of different surface roughness conditions was tested on the vertical isolated case, considered the fundamental scenario. These simulations reflect the dynamics observed in real downburst events. Time-frequency energy maps were used to identify frequency bands associated with the passage of the PV, typically around 1 Hz, and with the subsequent higher-mode trailing vortices (TVs). The analysis also detected the increased turbulence caused by the detachment of the boundary layer and the interaction of the PV with a secondary counter-rotating vortex (SV). Significant differences in the energy spectra were observed among the various cases, particularly in relation to the recording location. The variation of the energy spectra with height during the passage of the PV at maximum velocity provided valuable insights into the vertical motion of the vortex, whether it is rising or lowering in response to different simulated flow interactions. Furthermore, cross correlation analysis of wavelet signals from different heights, compared to the reference signal at the lowest measurement point below the PV, revealed phase angle shifts. In some cases, these shifts indicated a flow reversal, suggesting that the measurement height was above the vortex's upper end, where the flow is counter-directed relative to the flow below the PV. This analysis provides essential qualitative and quantitative information on vortex size, which is often overlooked in laboratory experiments that rely solely on pressure probes for flow measurement.

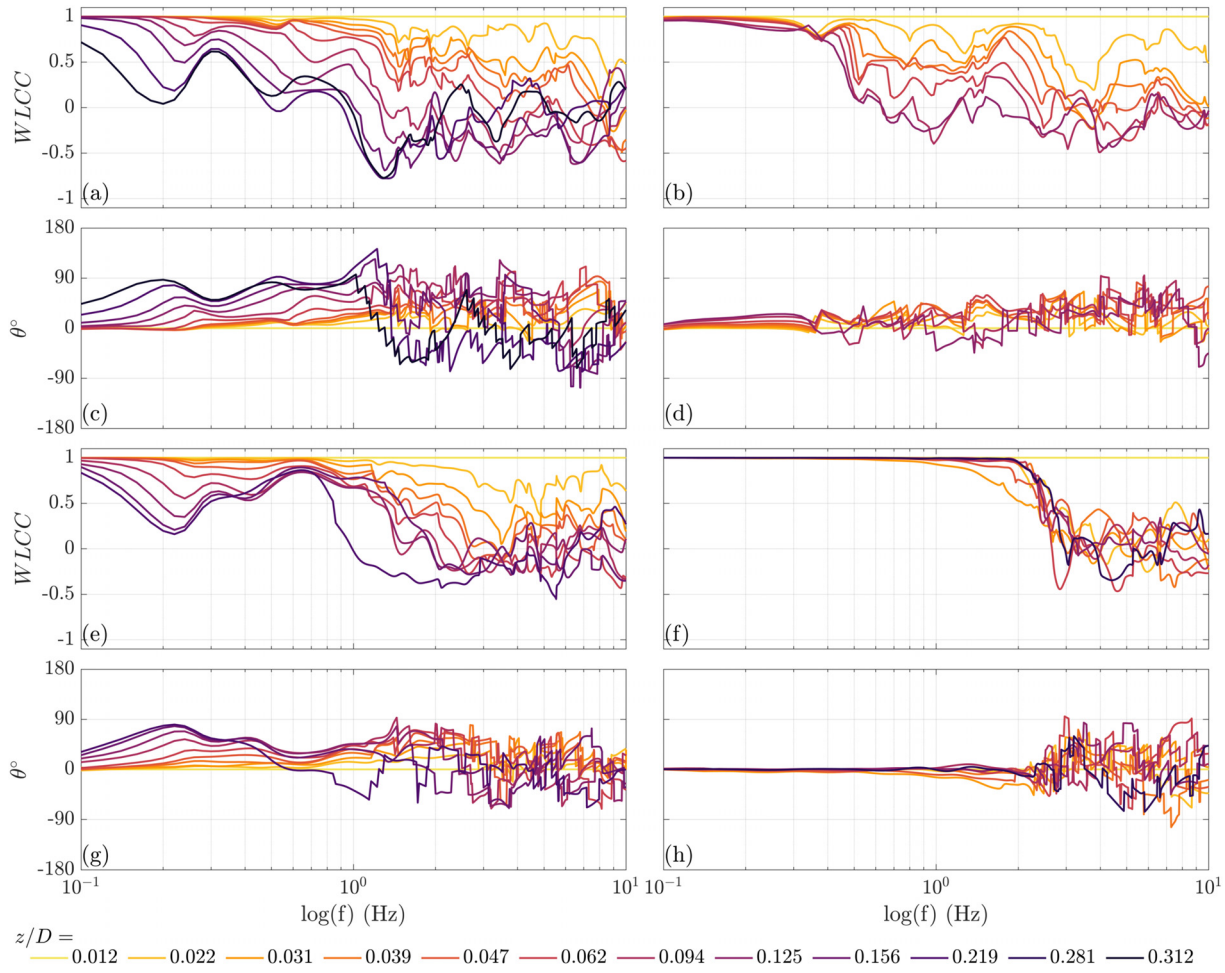

FIG. 14. Same as Fig. 13 but at $r/D = 1.6$.

The technique described in this paper will be further applied to databases of full-scale downburst events recently recorded in the Northern Mediterranean Sea (Canepa *et al.*, 2020; Canepa *et al.*, 2024b) to explore analogies and differences with the controlled simulations at the WindEEE Dome. The outcomes will contribute to the development of a framework that incorporates time-frequency analysis parameters, enabling more accurate downburst identification and extraction from large wind record databases. This approach will also enhance the representation and modeling of extreme wind events, supporting the standardization of downburst actions within meteorological practices and design codes, in particular, concerning sets of force and pressure coefficients. In fact, recent investigations conducted in uni-directional accelerating flows typical of downbursts on prismatic sharp-edged structures have unveiled aerodynamic characteristics that differ from those induced by stationary conditions. Notably, these differences affect the alternate nature of the vortex-shedding phenomenon (e.g., Brusco *et al.*, 2022b; Lunghi *et al.*, 2024 for a square cylinder), leading to discrepancies in the aerodynamic loading (e.g., Yang and Mason, 2019; Brusco *et al.*, 2024; and Chen *et al.*, 2025). Investigating these aspects under the action of complicated three-dimensional flows typical of downbursts is crucial. This methodology can help identify the vortical structures of the phenomenon that have the greatest impact as far as structural safety is concerned.

ACKNOWLEDGMENTS

The authors thank the organization of the "26th International Congress of Theoretical and Applied Mechanics," hosted by the International Union of Theoretical and Applied Mechanics in Daegu, South Korea, held over 25–30 August 2024, for creating the platform at which, and for bringing together the audience to which, this work was first presented.

This study was carried out within the RETURN Extended Partnership and received funding from the European Union Next-Generation EU (National Recovery and Resilience Plan—NRRP, Mission 4, Component 2, Investment 1.3—D.D. 1243 2/8/2022, No. PE0000005). The support of the European Research Council (ERC) under the European Union's Horizon 2020 research and innovation program (Grant Agreement No. 741273) for the project THUNDERR—Detection, simulation, modeling,

and loading of thunderstorm outflows to design wind-safer and cost-efficient structures—awarded with an Advanced Grant 2016 is acknowledged. Support from the Canada Foundation for Innovation (CFI) WindEEE Dome Grant (No. X2281B38) is also acknowledged.

AUTHOR DECLARATIONS

Conflict of Interest

The authors have no conflicts to disclose.

Author Contributions

Federico Canepa: Conceptualization (lead); Data curation (lead); Formal analysis (lead); Investigation (lead); Methodology (equal); Software (equal); Validation (lead); Visualization (lead); Writing – original draft (lead); Writing – review & editing (lead). **Hao-Yu Bin:** Conceptualization (equal); Formal analysis (equal); Methodology (equal); Software (lead); Validation (equal); Visualization (lead); Writing – review & editing (equal). **Stefano Brusco:** Conceptualization (equal); Formal analysis (equal); Methodology (equal); Software (lead); Writing – review & editing (equal).

DATA AVAILABILITY

The data that support the findings of this study are available from the corresponding author upon reasonable request.

REFERENCES

Allen, J. T., "Climate change and severe thunderstorms," in *Oxford Research Encyclopedia of Climate Science* (Oxford University Press, 2018).

Brusco, S., Buresti, G., and Piccardo, G., "Thunderstorm-induced mean wind velocities and accelerations through the continuous wavelet transform," J. Wind Eng. Ind Aerodyn. **221**, 104886 (2022a).

Brusco, S., Buresti, G., Lo, Y.-L., and Piccardo, G., "Constant-frequency time cells in the vortex-shedding from a square cylinder in accelerating flows," J. Wind Eng. Ind Aerodyn. **230**, 105182 (2022b).

Brusco, S., Bagnara, A., Cammelli, S., and Piccardo, G., "Experimental investigations on the vortex-shedding from a highly tapered circular cylinder in smooth flow," J. Fluids Struct. **122**, 103983 (2023).

Brusco, S., Bin, H.-Y., Lo, Y.-L., and Piccardo, G., "Transient aerodynamics of a square cylinder under downburst-like accelerating flows reproduced in a multiple-fan wind tunnel," J. Fluids Struct. **124**, 104038 (2024).

Buresti, G., Lombardi, G., and Bellazzini, J., "On the analysis of fluctuating velocity signals through methods based on the wavelet and Hilbert transforms," Chaos Solitons Fractals **20**, 149–158 (2004).

Burlando, M., Zhang, S., and Solari, G., "Monitoring, cataloguing, and weather scenarios of thunderstorm outflows in the northern Mediterranean," Nat. Hazards Earth Syst. Sci. **18**, 2309–2330 (2018).

Canepa, F., Burlando, M., and Solari, G., "Vertical profile characteristics of thunderstorm outflows," J. Wind Eng. Ind Aerodyn. **206**, 104332 (2020).

Canepa, F., Burlando, M., Hangan, H., and Romanic, D., "Experimental investigation of the near-surface flow dynamics in downburst-like impinging jets immersed in ABL-like winds," Atmosphere **13**, 621 (2022a).

Canepa, F., Burlando, M., Romanic, D., Solari, G., and Hangan, H., "Experimental investigation of the near-surface flow dynamics in downburst-like impinging jets," Environ. Fluid Mech. **22**, 921–954 (2022b).

Canepa, F., Burlando, M., Romanic, D., Solari, G., and Hangan, H., "Downburst-like experimental impinging jet measurements at the WindEEE Dome," Sci. Data **9**, 243 (2022c).

Canepa, F., Romanic, D., Hangan, H., and Burlando, M., "Experimental translating downbursts immersed in the atmospheric boundary layer," J. Wind Eng. Ind Aerodyn. **243**, 105570 (2023).

Canepa, F., Burlando, M., Romanic, D., and Hangan, H., "Effect of surface roughness on large-scale downburst-like impinging jets," Phys. Fluids **36**, 036610 (2024a).

Canepa, F., Repetto, M. P., and Burlando, M., "Full-scale measurements of thunderstorm outflows in the Northern Mediterranean," Geosci. Data J. **11**, 742 (2024b).

Chen, X.-Y., Zhu, L.-D., and Tan, Z.-X., "Influencing rule of accelerating flow's key parameters on unsteady aerodynamic forces of a 3:2 rectangular prism," Phys. Fluids **37**, 014118 (2025).

ESDU, "Strong winds in the atmospheric boundary layer. Part 1: Hourly-mean wind speeds," ESDU 82026 (ESDU, 2002).

Fujita, T. T., *The Downburst—Microburst and Macroburst: Report of Projects NIMROD and JAWS* (Satellite and Mesometeorology Research Project, Department of the Geophysical Sciences, University of Chicago, 1985).

Hangan, H., Refan, M., Jubayer, C., Romanic, D., Parvu, D., LoTufo, J., and Costache, A., "Novel techniques in wind engineering," J. Wind Eng. Ind Aerodyn. **171**, 12–33 (2017).

Hjelmfelt, M. R., "Structure and life cycle of microburst outflows observed in Colorado," J. Appl. Meteorol. Climatol. **27**, 900–927 (1988).

Junayed, C., Jubayer, C., Parvu, D., Romanic, D., and Hangan, H., "Flow field dynamics of large-scale experimentally produced downburst flows," J. Wind Eng. Ind Aerodyn. **188**, 61–79 (2019).

Lombardo, F. T., Smith, D. A., Schroeder, J. L., and Mehta, K. C., "Thunderstorm characteristics of importance to wind engineering," J. Wind Eng. Ind Aerodyn. **125**, 121–132 (2014).

Lombardo, F. T. and Zickar, A. S., "Characteristics of measured extreme thunderstorm near-surface wind gusts in the United States," J. Wind Eng. Ind Aerodyn. **193**, 103961 (2019).

Lunghi, G., Brusco, S., Mariotti, A., Piccardo, G., and Salvetti, M. V., "Influence of inflow acceleration on the aerodynamic characteristics of a square cylinder," J. Wind Eng. Ind Aerodyn. **252**, 105814 (2024).

Mariotti, A., "Axisymmetric bodies with fixed and free separation: Base-pressure and near-wake fluctuations," J. Wind Eng. Ind Aerodyn. **176**, 21–31 (2018).

Rädler, A. T., Groenemeijer, P. H., Faust, E., Sausen, R., and Púčik, T., "Frequency of severe thunderstorms across Europe expected to increase in the 21st century due to rising instability," Npj Clim. Atmos. Sci **2**, 30 (2019).

Romanic, D. and Hangan, H., "Experimental investigation of the interaction between near-surface atmospheric boundary layer winds and downburst outflows," J. Wind Eng. Ind Aerodyn. **205**, 104323 (2020).

Romanic, D., LoTufo, J., and Hangan, H., "Transient behavior in impinging jets in crossflow with application to downburst flows," J. Wind Eng. Ind Aerodyn. **184**, 209–227 (2019).

Romanic, D., Nicolini, E., Hangan, H., Burlando, M., and Solari, G., "A novel approach to scaling experimentally produced downburst-like impinging jet outflows," J. Wind Eng. Ind Aerodyn. **196**, 104025 (2020).

Solari, G., Burlando, M., De Gaetano, P., and Repetto, M. P., "Characteristics of thunderstorms relevant to the wind loading of structures," Wind Struct. **20**, 763–791 (2015).

Yang, T. and Mason, M. S., "Aerodynamic characteristics of rectangular cylinders in steady and accelerating wind flow," J. Fluids Struct. **90**, 246–262 (2019).

Zhang, S., Solari, G., De Gaetano, P., Burlando, M., and Repetto, M. P., "A refined analysis of thunderstorm outflow characteristics relevant to the wind loading of structures," Probab. Eng. Mech. **54**, 9–24 (2018).

Žužul, J., Ricci, A., Burlando, M., Blocken, B., and Solari, G., "Vortex dynamics and radial outflow velocity evolution in downburst-like winds," Comput. Fluids **283**, 106393 (2024).